New Materials, Compounds and Applications
Vol.9, No.3, 2025, pp.439-454
https://doi.org/10.62476/nmca.93439

EFFECT OF MORPHOLOGY ON LUMINESCENCE AND ANTIBACTERIAL ACTIVITY OF EUROPIUM DOPED HYDROXYAPATITE PARTICLES

Giovanni García-Domínguez[1], Joan Reyes-Miranda[2], Antonieta García-Murillo[3], Aristeo Garrido-Hernández[2*]

[1]Universidad Tecnológica Fidel Velázquez, Emiliano Zapata S/N, El Trafico, Cdad. Nicolás Romero, Estado de México, México
[2]Departamento de Materiales, Área Ciencia de los Materiales, Universidad Autónoma Metropolitana-Azcapotzalco, Av. San Pablo No. 420 Col. Nueva el Rosario C.P. 02128 Alcaldía Azcapotzalco, CDMX
[3]CIITEC IPN-Instituto Politécnico Nacional, Cerrada de Cecati s/n, Col. Santa Catarina, Azcapotzalco, Ciudad de Mexico, Mexico

Abstract. Eu-doped hydroxyapatite (HA:Eu) powders with spheres, rods and plates morphologies were synthesized via the solvothermal method. The structural and morphological properties of the samples were analyzed using X-ray diffraction (XRD) and scanning electron microscopy (SEM). Vibrational properties were investigated through Fourier-transform infrared (FT-IR) spectroscopy and photoluminescence (PL) studies. XRD analysis confirmed that all HA:Eu samples crystallized in a pure hexagonal phase without secondary phases, with a calculated crystallite size of approximately 20 nm. FT-IR spectra exhibited the characteristic vibrational bands of stoichiometric HA. Luminescence studies revealed that the luminescence originates from Eu^{3+} ions occupying the Ca^{2+}(I) sites in the HA lattice. The morphology of the particles had a significant influence on the emission intensity and transition efficiency, with spherical particles (HA-S) showing the highest photoluminescence due to enhanced Eu^{3+} site occupancy and minimized scattering effects, while rod- and plate-like structures exhibited reduced emission intensity.

Keywords: *Europium-doped hydroxyapatite, solvothermal synthesis, photoluminescence, particle morphology.*

Corresponding Author: *Aristeo Garrido-Hernández, Departamento de Materiales, Área Ciencia de los Materiales, Universidad Autónoma Metropolitana-Azcapotzalco, Av. San Pablo No. 420 Col. Nueva el Rosario C.P. 02128 Alcaldía Azcapotzalco, CDMX, Tel.: 5553189000, e-mail: agh@azc.uam.mx*

Received: *18 July 2025;* ***Accepted:*** *16 October 2025;* ***Published:*** *4 December 2025.*

1. Introduction

Hydroxyapatite (HA, $Ca_{10}(PO_4)_6(OH)_2$) belongs to the family of apatites characterized by the general formula $Ca_{10}(PO_4)_6X_2$, where X is a fluorine ion, chlorine or a hydroxyl group. Natural HA in the hexagonal phase is the main inorganic component of bones (Szcześ *et al*., 2017). Due to its excellent biocompatibility and bioactivity, HA has gained significant attention for a wide range of biomedical applications (Cao *et al*., 2010). In this context, synthetic HA plays a crucial role and has been extensively studied and produced through various synthesis routes. Although synthetic HA particles generally exhibit similar chemical compositions, precise control over their particle size and morphology is essential for specific applications such as bone tissue engineering (Zakaria *et al*., 2013), anticancer and antibacterial therapies (Canal *et al*., 2013; Bose &

Tarafder, 2012) and cellular imaging (Wagner *et al*., 2013). Consequently, considerable research has focused on tailoring HA morphologies, achieving structures such as nanoparticles, nanorods, nanocables, nanoflakes, hollow microspheres and flower-like architectures. To obtain these diverse nanostructures, several soft-chemical synthesis strategies have been developed, including hydrothermal (Neira *et al*., 2009; Nathanael *et al*., 2011) and co-precipitation methods (Aizawa *et al*., 2006). Key synthesis parameters such as pH, reaction time, co-solvent and precursor concentration - have been shown to significantly influence both the crystal structure and the morphology of HA particles, enabling fine control over their size and shape to meet specific functional requirements. Among the various techniques explored for controlling crystal morphology, the hydrothermal method has proven to be one of the most effective (Prakash *et al*., 2006; Gashti *et al*., 2013). It is widely applied in the synthesis of doped HA with different shapes and sizes, particularly one-dimensional nanorods and two-dimensional (2D) and three-dimensional (3D) nanoplate-assembled structures (Sadat-Shojai *et al*., 2013). Under hydrothermal treatment, these complexes can transform into hydroxyapatite (HA) through a dissolution-recrystallization mechanism (Mizutani *et al*., 2005). The nucleation and growth of HA are influenced by several factors, including organic additives, pH and ion concentrations. One effective strategy to modify HA morphology involves the use of co-solvents or surfactants during hydrothermal synthesis. Surfactants such as CTAB have been employed to control particle size and direct the formation of rod-like morphologies. One-dimensional nanostructures such as nanowires and nanorods have also been obtained through surfactant-assisted synthesis (Sans *et al*., 2021). Glycerol has emerged as an alternative co-solvent, which can modulate crystal growth by altering surface tension and reagent solubility, thereby influencing nucleation and growth behavior during the hydrothermal process.

In addition to controlling morphology, size and structure, another important route to enhance the functional properties of HA involves the incorporation of dopant atoms that modify HA's composition. These dopants can significantly enhance properties such as bioactivity, mechanical strength, antibacterial activity and luminescence (Motskin *et al*., 2009; Rahavi *et al*., 2017). A common strategy for improving mechanical and biological performance is the substitution of calcium ions with other metal ions such as Ag^{+} (Chen *et al*., 2016), Cu^{2+} (Shi *et al*., 2017) and Zn^{2+} (Iqbal *et al*., 2014). These dopants not only improve mechanical properties but also confer specific functionalities; for example, Zn^{2+} doping enhances osteoblast adhesion (Ghorbani *et al*., 2015), while Y^{3+} doping has been investigated for its application in humidity sensors due to its high-water affinity (Owada *et al*., 1989).

For luminescent and imaging applications, the incorporation of lanthanide ions, such as europium (Eu^{3+}), into the HA lattice has demonstrated considerable potential due to their unique optical properties. Europium, a red-emitting lanthanide, is widely used in high-efficiency fluorescent lamps (Ternane & Piriou, 1999), as a structural probe (Doat *et al*., 2005) and in biological labeling due to its high luminescence, low toxicity and biocompatibility (Jadalannagari *et al*., 2014; Hashemi *et al*., 2020; Chen *et al*., 2011; Han *et al*., 2010). In biomedical applications, Eu^{3+}-doped HA (HA:Eu) has been explored for applications such as drug delivery systems targeting specific cells or tissues (Chen *et al*., 2016) and implantable luminescent materials (Han *et al*., 2010). To be effective in these applications, HA:Eu materials must exhibit desirable characteristics such as controlled morphology, uniform particle size, large surface area and good dispersibility.

The previous studies discussed above have shown that Eu^{3+} emission in hydroxyapatite can be tailored through dopant concentration, calcination temperature or the presence of secondary phases. However, these works often did not isolate the role of particle morphology as a variable, making it difficult to isolate its effect from other synthesis parameters. In contrast, the present study focuses on systematically correlating three distinct morphologies (spheres, rods and plates) with their luminescence behavior and antibacterial performance, thus providing new insights into how shape and particle size modulate Eu^{3+} site occupancy and symmetry within the HA lattice, synthesized via a glycerol-assisted hydrothermal method.

2. Experimental

2.1. Synthesis

In the HA syntheses, a commercial grade of calcium nitrate tetrahydrate $CaNO_3•4H_2O$ (Mallinckrodt 99%), Diammonium and hydrogen phosphate $(NH_4)_2HPO_4$, (Baker Analyzed 98.7%) were used in the hydrothermal synthesis as starting materials. Glycerol (CIVEQ, ≥ 99.5%) was used as a co-solvent. $(NH_4)_2HPO_4$ solution at 0.5 M was added dropwise to $CaNO_3•4H_2O$ solution at 0.5 M; during the addition, the Ca solution was kept under stirring at 50 °C. To obtain 5 mol% of Eu^{3+} doped HA, Eu_2O_3 was dissolved in distilled water and then incorporated into the Ca Solution. Then, the final solution was adjusted at pH=11, using NaOH solution (1.5 M). Subsequently, the final solution was poured into a Teflon® lined autoclave at 200 °C for 15 h. The powders obtained were washed with ethanol and distilled water to ensure the complete removal of residual glycerol using a centrifuge (10000 rpm, 15 min. each wash). Finally, these powders were dried in an oven at 120°C. This procedure has been shown to effectively eliminate organic residues from solvothermal products, yielding phase-pure HA:Eu samples.

The concentration of glycerol used as a co-solvent was varied (15 and 30 wt%), as it is known to influence particle morphology. In the HA synthesis without glycerol, predominantly spherical particles were obtained; these samples were labeled as HA-S. When glycerol was added at 15 wt%, the resulting particles exhibited a rod-like morphology and were designated as HA-R. Finally, at a glycerol content of 30 wt%, the morphology shifted to large plate-like structures and the samples were named HA-P. The overall reaction yield was approximately 85% with respect to the stoichiometric amount of HA expected from the precursors.

2.2. Structural and morphological characterizations

X-ray diffraction (XRD) patterns were recorded at room temperature using a Bruker D8 Advance Eco diffractometer with Cu Kα (λ=1.54184 Å). The crystalline phases of the samples were determined by scanning over a 2θ range of 10-60°. Fourier-transform infrared (FTIR) spectra were obtained at room temperature using a Spectrum Two spectrophotometer. Each spectrum was recorded with 32 scans in the range of 4000-450 cm^{-1}. Scanning electron microscopy (SEM) micrographs were acquired using a JEOL JSM-7800F Scanning electron microscope under high vacuum conditions, operating at a low accelerating voltage of 5 kV.

2.3. Antibacterial activity

One of purpose was to evaluate the antimicrobial activity of hydroxyapatite particles HA and HA:Eu with different morphologies since it has been reported that the Eu^{3+} promotes antibacterial activity in the HA. The antibacterial assessment was conducted using the Kirby-Bauer disk diffusion method (Bauer *et al*., 1966). A positive control was conducted using a disk substrate containing 120 mg of mextesol-trimethoprim sulfate. *Staphylococcus aureus* (S. aureus 0364) and *Escherichia coli* (E. coli ATCC 25922) were selected as representative Gram-positive and Gram-negative bacteria, respectively. Both bacterial strains were grown on nutrient agar at 35±1 °C. Prior to microbiological experimentation, all glassware and samples were sterilized by autoclaving at 120 °C for 30 min. The antimicrobial activity of HA:Eu was assessed by preparing a suspension containing 100 μL of microbial cells suspended in 1 mL of Mueller-Hinton agar solution. Sensidisks were impregnated with 0.5 mg of HA particles dispersed in 1 mL of sterile water and placed on the agar plates containing the bacterial suspension. The plates were incubated at 35 °C for 24 hours. After incubation, the zones of inhibition around the disks were measured and the diameters of the sterile zones were recorded to evaluate the antimicrobial activity of the HA and HA:Eu samples.

3. Results and discussion

Figure 1 presents SEM images of hydroxyapatite (HA) samples synthesized with varying concentrations of glycerol. In the sample HA-S, synthesized without glycerol, agglomerated spherical particles were observed, with an average diameter of 0.56 ± 0.128 μm. When 15 wt% glycerol was used (HA-R), the particles exhibited a rod-like morphology, with an average length of 0.209 ± 0.04 μm. Increasing the glycerol concentration to 30 wt% (HA-P) resulted in the formation of plate-like particles with an average length of 26.25 ± 6.59 μm.

These results indicate that glycerol acts as a morphology-modifying agent, likely due to its effect on the surface tension of the synthesis medium. Indeed, several studies have suggested that both the crystalline structure and the nature of the matrix significantly influence particle morphology. For instance, in materials such as gadolinium ortophosphate with a hexagonal structure, morphology can be tuned by adjusting parameters such as glycerol content and pH (Hernández *et al*., 2014).

Figure 1 shows a significant increase in particle size from approximately 200 nm to about 25 μm with the addition of glycerol, which acts as a co-solvent that alters nucleation and crystal growth dynamics. It is observed that incorporating 15 wt% glycerol slightly modifies the morphology, resulting in nanorods, while increasing the concentration to 30 wt% leads to a shift toward two-dimensional (2D) and microscale structures. Glycerol influences the formation of HA:Eu by increasing the solution's viscosity, which reduces nucleation rates and promotes anisotropic growth, resulting in larger particles. At lower glycerol concentrations, nucleation occurs rapidly, generating a high density of small nuclei that limit individual crystal growth, thereby producing nanoparticles (~200 nm). In contrast, higher glycerol concentrations stabilize precursor ions in solution, suppress nucleation and facilitate prolonged crystal growth, resulting in larger microstructures (~25 μm). This trend is consistent with previous reports on polyol-assisted HA synthesis, where organic additives were shown to modulate growth kinetics (Qi *et al*., 2014; Sadat-Shojai *et al*., 2013).

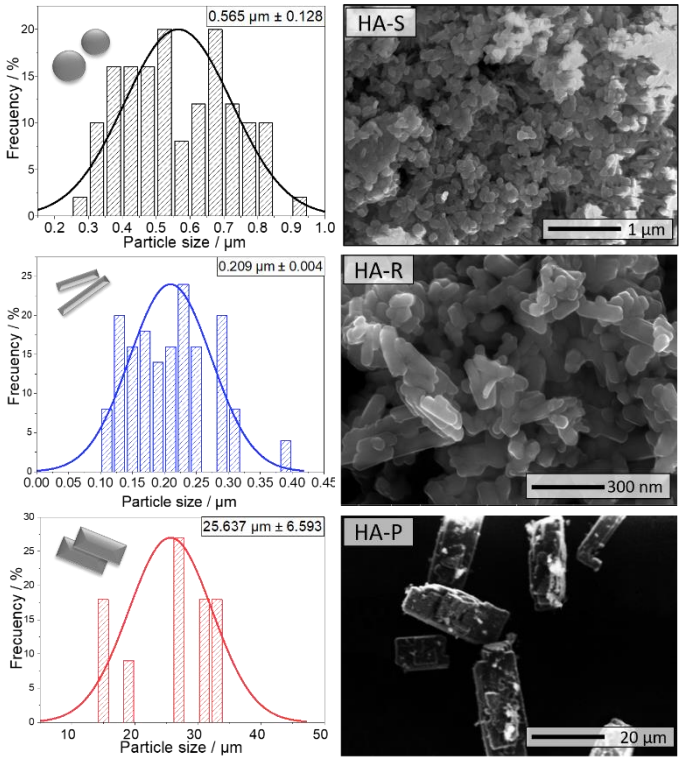

Figure 1. SEM micrographs of HA:Eu powders synthesized with varying glycerol concentrations showing (a) spherical morphology (HA-S), (b) rod-like morphology (HA-R) and (c) plate-like morphology (HA-P)

The phase structures of the synthesized HA samples were identified using X-ray diffraction (XRD). Figure 2 displays the corresponding diffractograms, where the observed peaks were indexed to the hexagonal phase of the hydroxyapatite with a space group P63/m, consistent with the reference pattern (ICDD 09-0432).

All of the powders exhibit good crystallinity; however, the samples synthesized with glycerol show a more pronounced peak around 26°, indicating a higher degree of crystallinity. The intensities of the (002), (102), (211) and (300) diffraction planes, located at 2θ = 25.97°, 26.5°, 31.93° and 32.93°, respectively, vary depending on the morphology of the HA samples. This variation is attributed to preferential crystal orientation promoted by the synthesis conditions, particularly the presence of glycerol as a solvent (Zhang *et al*., 2009). These observations support the earlier assertion that glycerol influences crystal orientation during synthesis. Furthermore, glycerol selectively interacts with specific crystallographic planes, modifying surface energies and directing growth into rod- and plate-like morphologies, as seen in the HA-R and HA-P samples. This anisotropic growth behavior has also been reported in other solvothermal syntheses of HA, where organic molecules preferentially stabilize certain crystal faces (Qi *et al*., 2014). An additional factor is the increased viscosity of the solution caused by glycerol, which slows the diffusion of Ca^{2+} and PO_4^{3-} ions, resulting in a more controlled and prolonged growth phase. Similar effects have been reported in polyol-mediated syntheses, where viscosity-induced control over crystal growth results in the formation of larger and more ordered structures (Baldassarre *et al*., 2020).

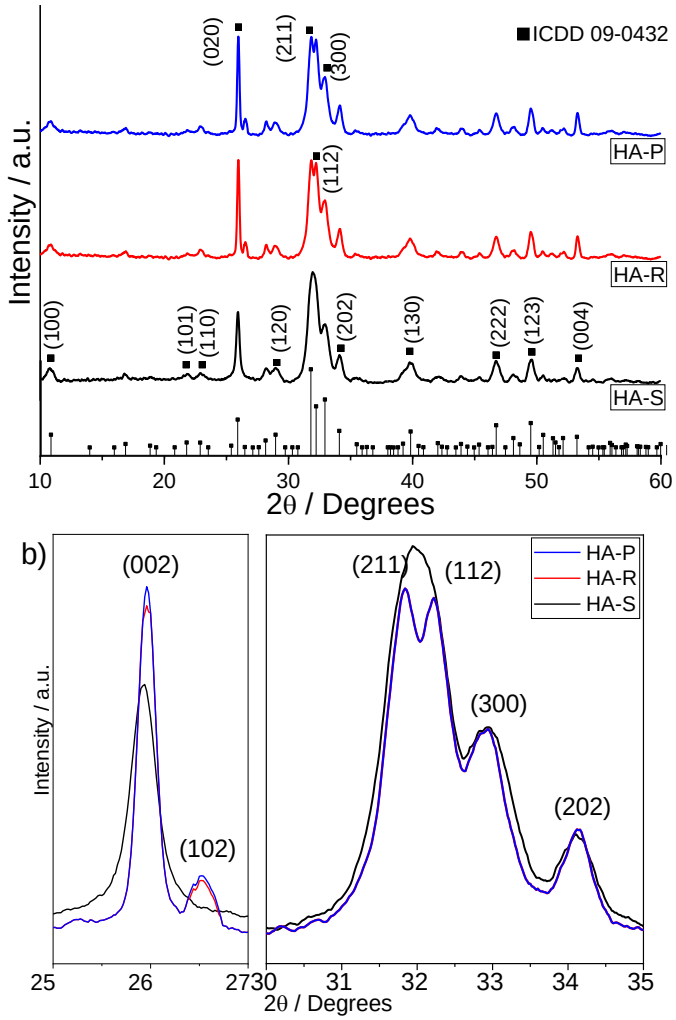

Figure 2. XRD patterns of HA:Eu particles with different morphologies: (a) full scan; (b) magnified region showing key diffraction planes (002, 211, 111, 300 and 202)

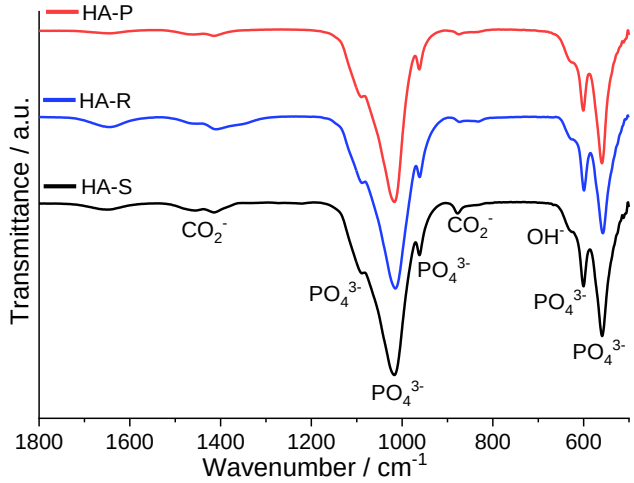

Figure 3. FTIR spectra of HA:Eu particles with spherical, rod-like and plate-like morphologies

As shown in Figure 3, the FTIR spectra reveal that all the synthesized HA samples exhibit similar spectral profiles. The characteristic absorption bands at 1094, 1017, 956,

604 and 560 cm^{-1} are attributed to the PO_4^{3-} ions in the HA structure. Specifically, the absorptions at 1094 and 1017 cm^{-1} correspond to the asymmetric stretching vibrations of the P-O bond within the phosphate group. The peak at 956 cm^{-1} is associated with the symmetric stretching mode of the P-O bond. Meanwhile, the peaks at 604 and 560 cm^{-1} are attributed to the bending vibrations of the O-P-O bonds. It is important to note that all the samples show absorption bands with similar intensities, indicating consistent structural characteristics across the synthesized HA samples.

Table 1 presents the total area occupied by the vibration bands and the relationship between the functional groups present in hydroxyapatite (HA). Rehman and Bonfield (1997) demonstrated that the structural quality and composition of HA can be effectively studied using infrared spectroscopy. In their study, they analyzed commercial HA particles synthesized through different methods and observed variations in the behavior of phosphate, carbonate and hydroxyl bands. Their findings confirmed a higher presence of carbonate residues in carbonate apatite compared to commercially synthesized hydroxyapatite samples. According to Murata et al. (1993) the incorporation of CO_3^{2-} ions into the HA structure occurs more frequently when water is present, making it less common in natural HA, such as that found in bones. The incorporation of CO_3^{2-} ions can have various consequences on the HA structure. The average reaction yield was estimated to be 85%, calculated by comparing the theoretical and experimental mass of the dried powder after washing and drying. The residual glycerol was effectively removed by repeated washing with absolute ethanol followed by distilled water until the pH of the supernatant reached neutrality. This washing protocol was validated by the absence of C-O stretching bands 1100-1000 cm^{-1} typically associated with glycerol in the FTIR spectra.

Table 1. Integrated FTIR vibrational band areas of PO_4^{3-}, OH^-, CO_3^{2-} and H_2O groups in HA:Eu samples with different morphologies

Wavenumber /cm^{-1}	Group	Area		
		HA-S	HA-R	HA-P
560	PO_4^{3-}	23.94	23.46	24.59
604	PO_4^{3-}	12.83	5.06	5.48
623	OH^-	6.25	4.15	7.08
956	PO_4^{3-}	6.98	1.80	3.63
1017	PO_4^{3-}	51.48	55.79	40.39
1094	PO_4^{3-}	28.75	23.28	35.66
1413	CO_2^-	1.80	9.08	0.84
1470	CO_2^-	11.55	11.75	0.78
1660	H_2O	1.70	4.66	0.30

In addition to phosphate and hydroxyl vibrations, all samples exhibited bands at ~1420 and ~870 cm^{-1}, which are assigned to the υ_3 and υ_2 modes of CO_3^{2-}, respectively. These features confirm B-type carbonate substitution, where CO_3^{2-} replaces PO_4^{3-} in the HA lattice. This substitution is commonly observed in wet chemical and hydrothermal syntheses (Rehman & Bonfield, 1997; Murata *et al.*, 1993) and is known to influence crystallinity, solubility and the local environment of substituent cations. Importantly, quantitative analysis of the band areas (Table 1) shows significant differences among morphologies: HA-R exhibited the highest carbonate content (CO_3^{2-}/PO_4^{3-} ratio ~0.16), HA-S an intermediate value (~0.13) and HA-P the lowest (~0.02). These variations suggest that particle morphology and size modulate the extent of carbonate incorporation, with rod-like particles being more prone to lattice substitution. Such substitution may

slightly distort the phosphate environment and consequently, alter the local symmetry around Eu^{3+} ions, thereby providing a mechanistic link between FTIR structural signatures and the luminescence behavior discussed later in this work.

The incorporation of Eu^{3+} ions into the crystalline HA structure was analyzed using photoluminescence (PL) spectroscopy. The excitation spectrum (Figure 4) was obtained by monitoring the emission wavelength at 590 nm and recorded in the range of 350-400 nm. The observed peaks are attributed to the f−f transitions of Eu^{3+}. The maximum excitation peak was found at 392 nm, with additional smaller peaks located at approximately 360, 374.3 and 380 nm. These peaks are associated with direct transitions from the ground state ($^7F_0$) of Eu^{3+} to higher energy levels in the [Xe]$4f^6$ electronic configuration, specifically the $^7F_0 \rightarrow {}^5D_4$ transition.

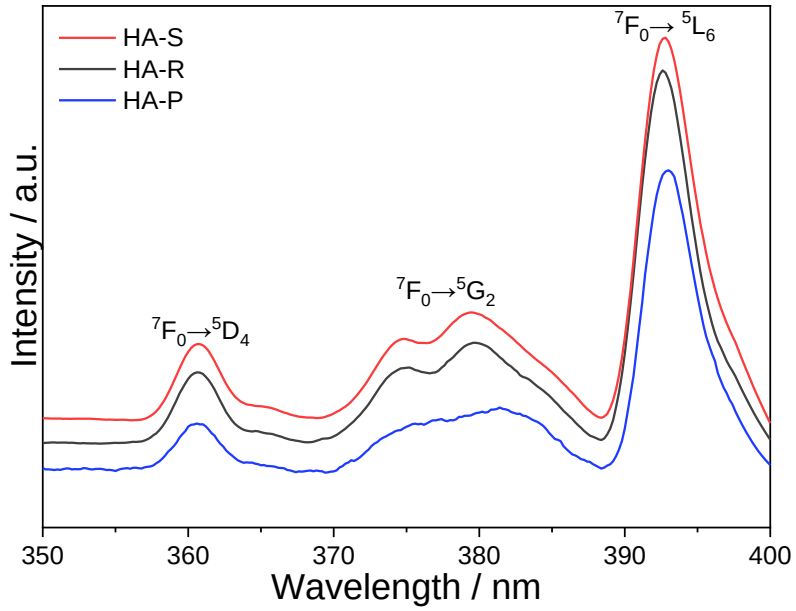

Figure 4. Excitation spectra of HA:Eu powders recorded at 590 nm, showing characteristic Eu^{3+} transitions and peak area analysis

The excitation spectra of Eu^{3+}-doped hydroxyapatite (HA:Eu) samples show a strong dependence on particle morphology, crystallinity and synthesis conditions. Among the studied morphologies, the sample synthesized without glycerol (HA-S) exhibits the highest excitation intensity, especially at 392 nm, while HA-R and HA-P display lower intensities across all excitation transitions.

Table 2. Integrated areas and relative percentages of Eu^{3+} excitation transitions in HA:Eu samples

Sample	Trans.	$^7F_0 \rightarrow {}^5D_4$	$^7F_0 \rightarrow {}^5G_2$		$^7F_0 \rightarrow {}^5L_6$	
	WL	**360**	**373**	**380**	**392**	**395**
HA-S	Area	0.782	0.542	2.414	3.253	1.645
	%	9.056	6.277	27.950	37.669	19.048
HA-R	Area	0.666	1.030	1.420	3.008	1.877
	%	8.328	12.868	17.748	37.597	23.458
HA-P	Area	0.856	0.382	2.782	3.100	1.915
	%	9.470	4.226	30.792	34.313	21.199

A consistent observation across all samples is the reduced intensity of the peak at 360 nm, corresponding to the $^7F_0 \rightarrow {}^5G_2$ transition. This decrease can be attributed to three main factors: a) *Crystal Anisotropy and Local Symmetry Alteration*. The solvothermal synthesis used for HA-R and HA-P promotes anisotropic crystal growth, altering the local symmetry of Eu^{3+} sites within the HA lattice. This distortion reduces the transition probabilities of certain excitation bands due to changes in the crystal field. Similar effects have been reported in lanthanide-doped phosphors, where more symmetric environments correlate with higher excitation intensities (Qi *et al*., 2014; Silva *et al*., 2015); b) *Particle Size and Optical Scattering*. Larger particles, particularly in HA-P (~25 μm), show evidence of self-absorption and increased optical scattering. These effects are more pronounced at shorter wavelengths, such as 360 nm, where the absorption cross-section is higher. As particle size increases, photon reabsorption and internal reflections become more likely, reducing overall excitation efficiency (Baldassarre *et al*., 2020; Farias *et al*., 2015); c) *Eu^{3+} Site Occupancy and Distribution*. Differences in Eu^{3+} incorporation efficiency further explain the spectral trends. HA-S, characterized by smaller and more uniform particles, likely provides more consistent and favorable sites for Eu^{3+} substitution into the Ca^{2+} lattice, resulting in higher excitation intensity. In contrast, HA-R and HA-P may feature site-selective incorporation due to their anisotropic structures, reducing the efficiency of certain transitions (Farias *et al*., 2015; Kim *et al*., 2018).

These interpretations are supported by data from Table 2, which shows that HA-R has the lowest relative intensities at 373 nm (12.86%) and 380 nm (17.74%). Additionally, differences in intensity ratios between key transitions (e.g., 32° and 46° XRD reflections for structural context, Figure 2) further highlight how particle morphology and crystallinity influence the ligand field and electronic environment around Eu^{3+} ions.

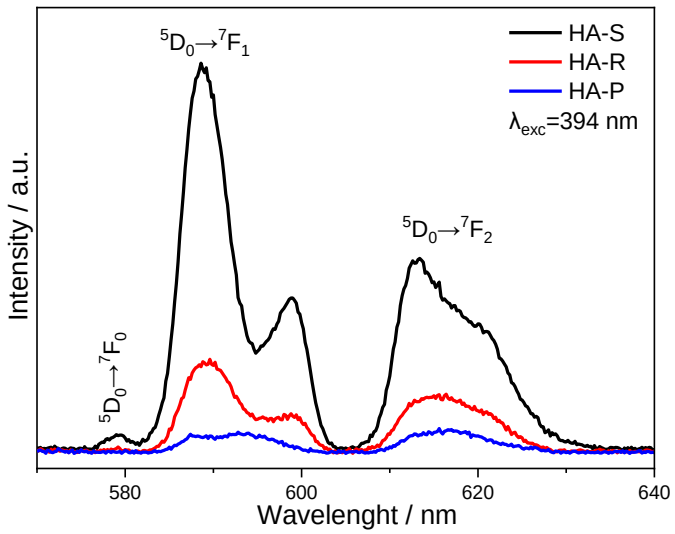

Figure 5. Emission spectra of HA:Eu particles with different morphologies under excitation at 394 nm

The emission spectra of the Eu^{3+}-doped HA samples excited at a wavelength of 394 nm are shown in Figure 5. All samples exhibit the characteristic Eu^{3+} emission lines, confirming successful dopant incorporation into the HA lattice. Among them, the spherical particles (HA-S) present the highest emission intensity, followed by the rod-like particles (HA-R) and finally, the plate-like structures (HA-P). Despite the intensity

differences, the three samples display the same emission bands, mainly associated with the $^5D_0 \rightarrow {}^7F_1$ transition at ~590 nm and the $^5D_0 \rightarrow {}^7F_2$ transition at ~612 nm.

These emission peaks, dominated by the $^5D_0 \rightarrow {}^7F_1$ band at ~590 nm, correspond to a magnetic-dipole transition, which is relatively insensitive to the local crystal field and therefore characteristic of Eu^{3+} ions located in high-symmetry environments. This confirms that Eu^{3+} preferentially occupies the Ca^{2+}(I) sites of the HA lattice, where the coordination environment is larger and more symmetric. In contrast, the weaker $^5D_0 \rightarrow {}^7F_2$ transition at ~612 nm, an electric-dipole hypersensitive transition, typically intensifies when Eu^{3+} ions are located in low-symmetry sites, such as Ca^{2+}(II). The relative weakness of this transition in the samples further supports the predominant substitution of Eu^{3+} at Ca^{2+}(I) positions, favored by the hydrothermal synthesis conditions, which stabilize dopant incorporation in sites of higher structural symmetry (Graeve *et al*., 2010; Silva *et al*., 2015).

The photoluminescence response of Eu^{3+}-doped HA is strongly dependent on the particle morphology, as confirmed by the correlation between SEM observations (Figure 1) and emission spectra (Figure 5). A clear hierarchy in emission intensity was established, with spherical particles (HA-S, 0.56 ± 0.13 μm) showing the highest luminescence, followed by rod-like structures (HA-R, 0.21 ± 0.04 μm) and finally plate-like particles (HA-P, 25.6 ± 6.6 μm) with the weakest emission.

This trend can be explained by considering particle size, local symmetry and Eu^{3+} site occupancy, as discused above. HA-S samples combine small submicrometric size with relatively homogeneous morphologies, favoring Eu^{3+} substitution at Ca^{2+}(I) lattice sites. This environment supports efficient magnetic-dipole ($^5D_0 \rightarrow {}^7F_1$) and electric-dipole ($^5D_0 \rightarrow {}^7F_2$) transitions, minimizing scattering losses and yielding the strongest emission intensity. HA-R particles, although smaller in size, display anisotropic growth along specific crystallographic directions. This anisotropy induces local field distortions and surface defects that increase non-radiative relaxation, which partially suppresses emission compared to spheres. HA-P particles, despite their larger crystallinity, exhibit the lowest luminescence due to their macroscopic dimensions, which enhance photon reabsorption and internal scattering and by promoting partial migration of Eu^{3+} ions toward less favorable Ca^{2+}(II) sites. Thus, morphology controls luminescence not only through optical scattering associated with particle size but also by modulating the crystal field symmetry and dopant site distribution. Similar correlations have been reported in Eu^{3+}-doped apatites and silicates (Graeve *et al*., 2010; Farias *et al*., 2015; Silva *et al*., 2015), but the present work demonstrates this dependence systematically across three distinct morphologies, positioning morphological control as a key strategy to tune the optical response of HA:Eu systems.

Additionally, impurities present in the material may act as activators, influencing the luminescence behavior and altering the relative intensities of the emission peaks. Yin et al. (2017) investigated the effect of calcination on the luminescence properties of Tb^{3+} doped HA particles doped with Tb^{3+}. Their study primarily highlighted the changes in the microstructure and local symmetry surrounding the Tb^{3+} ions induced by heat treatment. By reducing structural imperfections during calcination, the luminescence intensity initially increased, reaching a maximum as the calcination temperature approached 700 °C. Beyond this temperature, the luminescence intensity began to decline, although no evidence of HA particle decomposition was observed.

Although photoluminescence lifetime and absolute quantum yield were not measured, the emission analysis is reinforced by the asymmetry ratio $R = I_{(^5D_0 \rightarrow {}^7F_2)}/$

$I_{(^5D_0 \rightarrow ^7F_1)}$, a well-established proxy for the local symmetry around Eu^{3+}. The calculated values are R(HA-S) = 0.50, R(HA-R) = 0.64 and R(HA-P) = 1.16. Ratios < 1 (HA-S, HA-R) indicate dominance of the magnetic-dipole $^5D_0 \rightarrow ^7F_1$ transition and thus higher-symmetry environments consistent with Ca^{2+}(I) occupation; a ratio > 1 (HA-P) reflects a relative enhancement of the electric-dipole, hypersensitive $^5D_0 \rightarrow ^7F_2$ transition, evidencing lower symmetry/distortion and increased contribution of Ca^{2+}(II) sites. This systematic trend (HA-S < HA-R < HA-P) aligns with the SEM-derived morphologies and sizes, supporting the hypothesis of site-selective substitution and a preferential migration of Eu^{3+} from Ca^{2+}(I) to Ca^{2+}(II) sites, as also reported by Takaichi et al. (2010). These observations are consistent with prior reports that correlate Eu^{3+} luminescence with structural/morphological factors even in the absence of direct lifetime measurements (Mondal *et al*., 2012; Zhang *et al*., 2009).

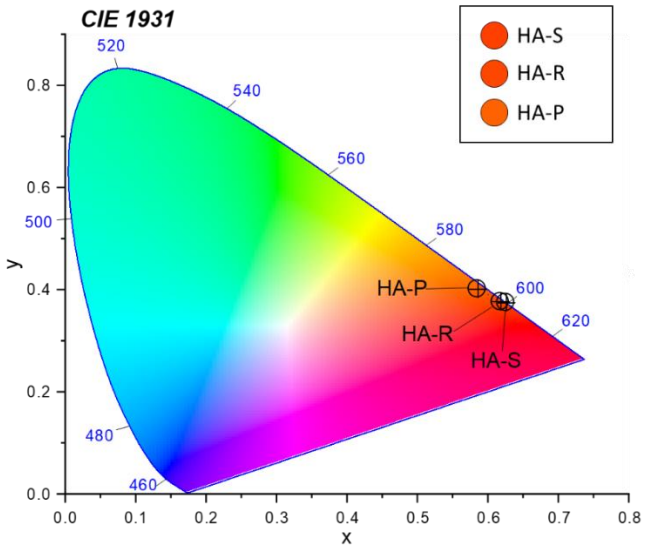

Figure 6. CIE chromaticity coordinates of HA:Eu samples under 394 nm excitation, indicating morphology-dependent emission color

The chromaticity coordinates of the Eu^{3+}-doped HA samples are shown in Figure 6 and summarized in Table 3. HA-S exhibits coordinates of (x = 0.5025, y = 0.3724) with a correlated color temperature (CCT) of 1886 K and a color purity of 83.25%, placing it deep in the red region of the CIE 1931 diagram. HA-R shows coordinates of (x = 0.4725, y = 0.3531), CCT of 2010 K and purity of 54.71%, while HA-P presents (x = 0.4362, y = 0.3492), CCT of 2486 K and purity of 41.81%. These results demonstrate a clear morphological dependence: spherical particles (HA-S) achieve the highest chromatic purity, whereas rod- and plate-like morphologies yield progressively lower purities and higher CCT values, shifting toward orange-red.

Kim et al. (2018) synthesized phosphosilicate particles doped with europium and successfully altered their emission color. They investigated the spectroscopic properties of the phosphors by varying their crystal structure. Specifically, the transition from a whitlockite to an apatite crystalline structure resulted in a change in the position of the Eu ions, altering their bonding distances with neighboring activator ions. Similarly, Farias et al. (2015) demonstrated that the luminescent properties of europium-doped

aluminosilicates can be modified by adjusting the symmetry of the Eu^{3+} ion sites through variations in silica concentration.

Table 3. CIE chromaticity coordinates (x, y), correlated color temperature (CCT), purity and emission color of HA:Eu samples

Sample	Chromatic coordinates (x, y)		CCT (K)	Purity (%)
HA-S	0.5025	0.3724	1886.19	83.25
HA-R	0.4725	0.3531	2010.22	54.71
HA-P	0.4362	0.3492	2486.15	41.81

Regarding to Eu^{3+}-based phosphors used for bioimaging ($Y_2O_3:Eu^{3+}$, $LaPO_4:Eu^{3+}$, $Gd_2O_3:Eu^{3+}$), which typically show chromatic coordinates in the range x ≈ 0.60-0.64, y ≈ 0.34-0.36 and purities above 80% (Nath *et al*., 2024; Ansari *et al*., 2017), the HA-S sample shows a comparable red emission profile. Although HA-R and HA-P are less pure, their coordinates remain within the orange-red spectral region, confirming that morphology significantly modulates colorimetric properties. Importantly, the high purity achieved by HA-S (83.25%) demonstrates that bioceramics can approach the optical quality of conventional oxide phosphors while retaining intrinsic biocompatibility.

Figure 7 displays the antibacterial activity results obtained through the Kirby-Bauer disk diffusion method, comparing HA:Eu samples. The observed inhibition zones for HA:Eu samples reached diameters greater than 15 mm. According to the interpretative criteria for antimicrobial susceptibility (≥15 mm → Sensitive (S) → microorganism inhibited; 11–14 mm → Intermediate (I) → partial inhibition; ≤10 mm → Resistant (R) → no effective inhibition), these values confirm that the HA:Eu samples exhibited a clear antibacterial effect (CLSI, 2024). Importantly, all experiments were performed in triplicate and inhibition halos greater than 15 mm were consistently observed in every repetition, confirming the reproducibility and reliability of the antibacterial response. These results clearly indicate that the enhanced antibacterial effect is attributable to the incorporation of europium ions into the HA matrix. Furthermore, the particle morphology - whether spherical, rod-like or plate-like - did not significantly affect the antimicrobial outcome, reinforcing that the activity is primarily governed by chemical composition rather than particle shape or size.

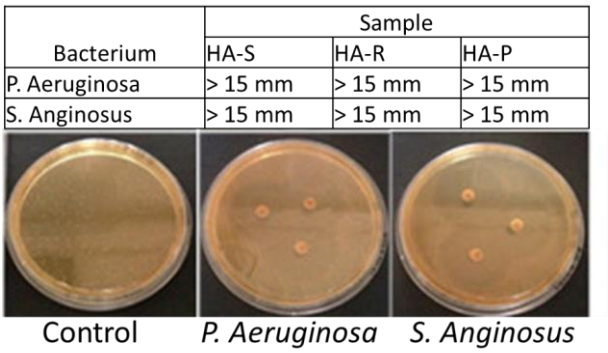

Figure 7. Antibacterial inhibition zones for HA:Eu particles against *P. aeruginosa* and *S. anginosus* using the disk diffusion method

The antimicrobial effect of europium is proposed to occur via two main mechanisms. First, Eu^{3+} ions may penetrate bacterial cells and interfere with intracellular

functions, including ATP synthesis and DNA replication, ultimately leading to cell death. Second, europium ions may accumulate at the bacterial membrane, disrupting its integrity, altering its permeability and causing the leakage of intracellular components such as proteins and polysaccharides. These mechanisms compromise essential cellular processes and structure, leading to effective bacterial inhibition. Taken together, these findings suggest that europium doping provides a valuable antibacterial enhancement to HA-based materials without the need for changes in particle morphology. Several mechanisms have been proposed to explain the antibacterial activity of europium. The first involves Eu^{3+} ions penetrating the bacterial cell and disrupting intracellular processes, such as adenosine triphosphate (ATP) production, which ultimately inhibits DNA replication (Mijnendonckx *et al*., 2013). The second mechanism is associated with the accumulation of Eu^{3+} ions on the bacterial cell membrane, altering its permeability. This results in the release of proteins and polysaccharides prevents proton transport across the membrane and ultimately leads to membrane destruction and bacterial cell death (Dastjerdi & Montazer, 2010; Darouiche *et al*., 1999).

4. Conclusion

This study demonstrates that the morphology of Eu^{3+}-doped hydroxyapatite particles, controlled via solvothermal synthesis with varying glycerol concentrations, significantly influences their luminescence and crystallinity, while exerting minimal effect on their antibacterial properties. Spherical particles (HA-S) exhibited the highest photoluminescence intensity, likely due to enhanced Eu^{3+} incorporation, reduced self-scattering and more symmetrical crystal fields. In contrast, rod-like (HA-R) and plate-like (HA-P) particles synthesized at higher glycerol concentrations showed diminished emission, attributed to increased crystal anisotropy, larger particle size and potential surface contamination from organic residues. Despite these morphological variations, all HA:Eu samples retained good structural integrity, as confirmed by XRD and FTIR analyses. Antibacterial assays revealed that europium incorporation notably enhanced microbial inhibition against both Gram-positive and Gram-negative bacteria, regardless of particle shape or size. These results indicate that antibacterial performance is primarily governed by the chemical composition of the HA matrix rather than morphology. The findings highlight the dual functionality of HA:Eu systems, which combine tunable optical properties with intrinsic antimicrobial activity. Such characteristics position these materials as promising candidates for advanced biomedical applications, including bioimaging, implantable devices and luminescent antibacterial coatings.

Acknowledgment

The authors gratefully acknowledge the support provided by the Centro de Cooperación Academia Industria (CCAI) of Universidad Tecnológica Fidel Velázquez (UTFV) for facilitating the experimental analysis. Special thanks are extended to the Department of Materials of Universidad Autónoma Metropolitana (UAM) for providing access to characterization instruments.

References

Aizawa, M., Ueno, H., Itatani, K. & Okada, I. (2006). Syntheses of calcium-deficient apatite fibres by a homogeneous precipitation method and their characterizations. *Journal of the*

European Ceramic Society, *26*(4-5), 501-507.

Ansari, A.A., Labis, J.P. & Manthrammel, M.A. (2017). Designing of luminescent $GdPO_4$:Eu@$LaPO_4$@SiO_2 core/shell nanorods: Synthesis, structural and luminescence properties. *Solid State Sciences*, 71, 117-122.

Baldassarre, F., Altomare, A., Corriero, N., Mesto, E., Lacalamita, M., Bruno, G., … & Siliqi, D. (2020). Crystal chemistry and luminescence properties of Eu-doped polycrystalline hydroxyapatite synthesized by chemical precipitation at room temperature. *Crystals*, *10*(4), 250.

Bauer, A.W., Kirby, W.M., Sherris, J.C. & Turck, M. (1966). Antibiotic susceptibility testing by a standardized single disk method. *American Journal of Clinical Pathology*, *45*(4), 493-496.

Bose, S., Tarafder, S. (2012). Calcium phosphate ceramic systems in growth factor and drug delivery for bone tissue engineering: A review. *Acta Biomaterialia*, *8*(4), 1401-1421.

Canal, C., Pastorino, D., Mestres, G., Schuler, P. & Ginebra, M.P. (2013). Relevance of microstructure for the early antibiotic release of fresh and pre-set calcium phosphate cements. *Acta Biomaterialia*, *9*(9), 8403-8412.

Cao, H., Zhang, L., Zheng, H. & Wang, Z. (2010). Hydroxyapatite nanocrystals for biomedical applications. *The Journal of Physical Chemistry C, 114*(43).

Chen, F., Zhu, Y., Ding, G., Wu, J. & Qi, C. (2011). Europium-doped amorphous calcium phosphate porous nanospheres: Preparation and application as luminescent drug carriers. *Nanoscale Research Letters*, *6*(1), 67.

Chen, S., Gururaj, S., Xia, W. & Engqvist, H. (2016). Synthesis of Ag doped calcium phosphate particles and their antibacterial effect as additives in dental glass ionomer cements. *Journal of Materials Science: Materials in Medicine, 27*(11), 172.

Ciobanu, C.S., Iconaru, S.L., Massuyeau, F., Constantin, L.V., Costescu, A. & Predoi, D. (2012). Synthesis, structure and luminescent properties of europium-doped hydroxyapatite nanocrystalline powders. *Journal of Nanomaterials*, 1, 942801.

Clinical and Laboratory Standards Institute (CLSI) (2024). *Performance Standards for Antimicrobial Susceptibility Testing*, 34th edition. CLSI M100, 416.

Darouiche, R.O., Raad, I.I., Heard, S.O., Thornby, J.I., Wenker, O.C., … & Mayhall, G.F. (1999). A comparison of two antimicrobial-impregnated central venous catheters. *The New England Journal of Medicine, 340*(1), 1-8.

Dastjerdi, R., Montazer, M. (2010). A review on the application of inorganic nano-structured materials in the modification of textiles: Focus on anti-microbial properties. *Colloids and Surfaces B: Biointerfaces*, *79*(1), 5-18.

Doat, A., Pellé, F. & Lebugle, A. (2005). Europium-doped calcium pyrophosphates: Allotropic forms and photoluminescent properties. *Journal of Solid State Chemistry, 178*(7), 2354-2362.

Farias, A.M., Sandrini, M., Viana, J.R.M., Baesso, M.L., Bento, A.C., Rohling, J.H. & Guyot, Y. (2015). Emission tunability and local environment in europium-doped OH^--free calcium aluminosilicate glasses for artificial lighting applications. *Materials Chemistry and Physics*, 156, 214-219.

Gashti, M.P., Bourquin, M., Stir, M. & Hulliger, J. (2013). Glutamic acid inducing kidney stone biomimicry by a brushite/gelatin composite. *Journal of Materials Chemistry B, 1*(10), 1501-1508.

Ghorbani, F.M., Kaffashi, B., Shokrollahi, P., Seyedjafari, E. & Ardeshirylajimi, A. (2015). PCL/chitosan/Zn-doped nHA electrospun nanocomposite scaffold promotes adipose-derived stem cells adhesion and proliferation. *Carbohydrate Polymers*, 118, 133-142.

Graeve, O.A., Kanakala, R., Madadi, A., Williams, B.C. & Glass, K.C. (2010). Luminescence variations in hydroxyapatites doped with Eu^{2+} and Eu^{3+} ions. *Biomaterials, 31*(15), 4259-4267.

Han, Y., Wang, X. & Li, S. (2010). Biocompatible europium doped hydroxyapatite nanoparticles

as a biological fluorescent probe. *Current Nanoscience, 6*(2), 178-183.

Hashemi, N., Kharaziha, M., Shafiei, S. & Nikkhah, M. (2020). A novel fluorescent hydroxyapatite based on iron quantum cluster template to enhance osteogenic differentiation. *Materials Science and Engineering: C,* 111, 110778

Hernández, A.G., Boyer, D., Potdevin, A., Chadeyron, G., Murillo, A.G., de J. Carrillo Romo, F. & Mahiou, R. (2014). Hydrothermal synthesis of lanthanide-doped $GdPO_4$ nanowires and nanoparticles for optical applications. *Physica Status Solidi A: Applications and Materials Science, 211*(2), 498-503.

Iqbal, N., Huang, K., Wang, F., Ali, S., Khan, Z. & Munir, A. (2014). Characterization, antibacterial and in vitro compatibility of zinc-silver doped hydroxyapatite nanoparticles prepared through microwave synthesis. *Ceramics International*, 40, 4507-4513.

Jadalannagari, S., Deshmukh, K., Verma, A., Vohra, R., Kowshik, M. & Ramanan, S. (2014). Lanthanum-doped hydroxyapatite nanoparticles as biocompatible fluorescent probes for cellular internalization and biolabeling. *Science of Advanced Materials, 6*(1), 312-319.

Kim, D., Moon, B.K., Park, S.H., Kim, J.H. & Jeong, J. H. (2018). Full-color tuning in europium-doped phosphosilicate phosphors via adjusting crystal field modulation or excitation wavelength. *Journal of Alloys and Compounds,* 770, 411-418.

Mijnendonckx, K., Leys, N., Mahillon, J., Silver, S. & Van Houdt, R. (2013). Antimicrobial silver: Uses, toxicity and potential for resistance. *BioMetals, 26*(4), 609-621.

Mizutani, Y., Hattori, M., Okuyama, M., Kasuga, T. & Nogami, M. (2005). Large-sized hydroxyapatite whiskers derived from calcium tripolyphosphate gel. *Journal of the European Ceramic Society*, *25*(13), 3181-3185.

Motskin, M., Wright, D.M., Muller, K., Kyle, N., Gard, T.G., Porter, A.E. & Skepper, J.N. (2009). Hydroxyapatite nano and microparticles: Correlation of particle properties with cytotoxicity and biostability. *Biomaterials, 30*(19), 3307-3317.

Mondal, S., Basu, B., & Balasubramanian, K. (2012). Europium-doped hydroxyapatite: luminescence properties and structural correlations. *Journal of Materials Science, 47*(3), 1500–1508

Murata, T., Kai, A. & Miki, T. (1993). Hydration effects on CO_2^- radicals in calcium carbonates and hydroxyapatite. *Applied Radiation and Isotopes, 44*(1-2), 305-309.

Nath, S.G., Jose, J., Bhat, S.G. & Anila, E.I. (2024). Labelling of human breast cancer cells with PEG/biotin encapsulated B-type Y_2O_3:Eu nanophosphors for fluorescence detection. *Inorganic Chemistry Communications*, 169, 113100.

Nathanael, A.J., Mangalaraj, D., Hong, S.I. & Masuda, Y. (2011). Synthesis and in-depth analysis of highly ordered yttrium doped hydroxyapatite nanorods prepared by hydrothermal method and its mechanical analysis. *Materials Characterization, 62*(12), 1109-1115.

Neira, I.S., Kolen'ko, Y.V., Lebedev, O.I., Van Tendeloo, G., Gupta, H.S., Guitián, F. & Yoshimura, M. (2009). An effective morphology control of hydroxyapatite crystals via hydrothermal synthesis. *Crystal Growth & Design*, *4*(1), 466-474.

Owada, H., Yamashita, K., Umegaki, T., Kanazawa, T. & Nagai, M. (1989). Humidity-sensitivity of yttrium-substituted apatite ceramics. *Solid State Ionics,* 35, 401-404.

Prakash, K.H., Kumar, R., Ooi, C.P., Cheang, P. & Khor, K.A. (2006). Apparent solubility of hydroxyapatite in aqueous medium and its influence on the morphology of nanocrystallites with precipitation temperature. *Langmuir*, *22*(6), 11002-11008.

Qi, C., Zhu, Y., Ding, G., Wu, J. & Chen, F. (2014). Solvothermal synthesis of hydroxyapatite nanostructures with various morphologies using adenosine 5′-monophosphate sodium salt as an organic phosphorus source. *RSC Advances,* 5, 3792-3798.

Rahavi, S.S., Ghaderi, O., Monshi, A. & Fathi, M.H. (2017). A comparative study on physicochemical properties of hydroxyapatite powders derived from natural and synthetic sources. *Russian Journal of Non-Ferrous Metals*, *58*(3), 276-286.

Rehman, I., Bonfield, W. (1997). Characterization of hydroxyapatite and carbonated apatite by photoacoustic FTIR spectroscopy. *Journal of Materials Science: Materials in Medicine, 8*(1), 1-4.

Sadat-Shojai, M., Khorasani, M., Dinpanah-Khoshdargi, E. & Jamshidi, A. (2013). Synthesis methods for nanosized hydroxyapatite in diverse structures. *Acta Biomaterialia*, *9*(8), 7591-7621.

Sans, J., Sanz, V., Puiggalí, J., Turon, P. & Alemán, C. (2021). Controlled anisotropic growth of hydroxyapatite by additive-free hydrothermal synthesis. *Crystal Growth & Design*, *21*(2), 748-756.

Shi, F., Liu, Y., Zhi, W., Xiao, D., Li, H., Duan, K., Qu, S. & Weng, J. (2017). The synergistic effect of micro/nano-structured and Cu^{2+}-doped hydroxyapatite particles to promote osteoblast viability and antibacterial activity. *Biomedical Materials*, *12*(3), 035006.

Silva, F.R.O., de Lima, N.B., Bressiani, A.H.A., Courrol, L.C. & Gomes, L. (2015). Synthesis, characterization and luminescence properties of Eu^{3+}-doped hydroxyapatite nanocrystals and the thermal treatment effects. *Optical Materials*, 47, 135-142.

Szcześ, A., Hołysz, L. & Chibowski, E. (2017). Synthesis of hydroxyapatite for biomedical applications. *Advances in Colloid and Interface Science*, 249, 321-330.

Ternane, R., Piriou, B. (1999). Luminescent properties of Eu^{3+} in calcium hydroxyapatite. *Materials Science and Engineering: B, 81*(1), 165-170.

Wagner, D.E., Eisenmann, K.M., Nestor-Kalinoski, A.L. & Bhaduri, S.B. (2013). A microwave-assisted solution combustion synthesis to produce europium-doped calcium phosphate nanowhiskers for bioimaging applications. *Acta Biomaterialia*, *9*(9), 8422-8432.

Yin, H.R., Li, Y.X., Bai, J.G., Qiao, Y.P., Liu, J., Pan, Z. & Gao, S. (2017). Effect of calcination temperature on the luminescence intensity and fluorescent lifetime of Tb^{3+}-doped hydroxyapatite nanocrystallines. *Journal of Materiomics*, *3*(2), 144-149.

Zakaria, S.M., Hussein, S., Zein, S., Othman, M.R., Yang, F. & Jansen, J.A. (2013). Nanophase hydroxyapatite as a biomaterial in advanced hard tissue engineering: A review. *Tissue Engineering Part B: Reviews*, *19*(5), 431-441.

Zhang, C., Yang, J., Quan, Z., Yang, P., Li, C., Hou, Z. & Lin, J. (2009). Hydroxyapatite nano- and microcrystals with multiform morphologies: Controllable synthesis and luminescence properties. *Crystal Growth and Design*, *9*(6), 2725-2733.